Efficient Shadow Detection of Color Aerial Images Based on Successive Thresholding Scheme

Kuo-Liang Chung, *Senior Member, IEEE*, Yi-Ru Lin, and Yong-Huai Huang

Abstract—Recently, Tsai presented an efficient algorithm which uses the ratio value of the hue over the intensity to construct the ratio map for detecting shadows of color aerial images. Instead of only using the global thresholding process in Tsai's algorithm, this paper presents a novel successive thresholding scheme (STS) to detect shadows more accurately. In our proposed STS, the modified ratio map, which is obtained by applying the exponential function to the ratio map proposed by Tsai, is presented to stretch the gap between the ratio values of shadow and nonshadow pixels. By performing the global thresholding process on the modified ratio map, a coarse-shadow map is constructed to classify the input color aerial image into the candidate shadow pixels and the nonshadow pixels. In order to detect the true shadow pixels from the candidate shadow pixels, the connected component process is first applied to the candidate shadow pixels for grouping the candidate shadow regions. For each candidate shadow region, the local thresholding process is performed iteratively to extract the true shadow pixels from the candidate shadow region. Finally, for the remaining candidate shadow regions, a fine-shadow determination process is applied to identify whether each remaining candidate shadow pixel is the true shadow pixel or not. Under six testing images, experimental results show that, for the first three testing images, both Tsai's and our proposed algorithms have better detection performance than that of the algorithm of Huang *et al.*, and the shadow detection accuracy of our proposed STS-based algorithm is comparable to Tsai's algorithm. For the other three testing images, which contain some low brightness objects, our proposed algorithm has better shadow detection accuracy when compared with the previous two shadow detection algorithms proposed by Huang *et al.* and Tsai.

Index Terms—Coarse-to-fine strategy, color aerial image, shadow detection, successive thresholding scheme (STS).

I. INTRODUCTION

IN URBAN aerial images, shadows usually result in information loss or distortion of objects [1], [2]; thus, it is an important research issue to detect shadows for urban aerial images. Based on the three features, which are intensity values, geometrical properties, and light directions, several efficient algorithms have been presented to detect shadows for gray aerial images [3]–[6]. Since gray aerial images only provide

the intensity information, some nonshadow regions may be identified as shadows even if the aforementioned three features have been considered. However, for color aerial images, the shadow detection accuracy can be improved by utilizing both the intensity and the color information.

Because the chromaticity information is not affected by the change of illumination for some cases, a shadow region can be detected by selecting the region which is darker than its neighboring regions but has similar chromaticity information. According to this illumination invariant property of chromaticity, several efficient methods [7]–[9] have been developed to detect shadows for color images efficiently. However, they may not work well for color aerial images since some shadow properties in color aerial images have not been considered. To detect shadows of color aerial images, Polidorio *et al.* [10] utilized two properties of shadows, which are the low luminance and the highly saturated blue/violet wavelength, to detect shadows. According to the two shadow properties, the red, green, and blue (*RGB*) color aerial image is first transformed into the hue, saturation, and intensity (*HSI*) color model, and then, a segmentation process is applied to the saturation component and the intensity component to identify shadows. Later, Huang *et al.* [11] observed that the pixels in a shadow region usually have large hue value, low blue color value, and small difference between green and blue color values. Following this observation, three experimental thresholds are determined to detect shadows in the *HSI* color model. Recently, Tsai [12] presented an efficient algorithm to detect shadows for color aerial images, too. The input image can be first transformed into the *HSI*; hue, saturation, and value (*HSV*); luma, blue-difference chroma, and red-difference chroma (YC_bC_r); hue, chroma, and value (*HCV*); or luminance, hue, and saturation (*YIQ*) color models. Under the transformed invariant color model, Tsai first calculated the ratio of the hue over the intensity for each pixel to construct the ratio map, and then, a global threshold of the constructed ratio map is determined to identify shadows. Experimental results show that Tsai's algorithm has better shadow detection accuracy when compared to the previous works [10], [11]. Note that, among these invariant color models, Tsai's algorithm has the best shadow detection performance for the *HSI* color model.

In this paper, a new successive thresholding scheme (STS) is proposed to detect shadows for color aerial images. Instead of using the ratio map by Tsai, our proposed modified ratio map, which is obtained by applying the exponential function to the ratio map, is presented to stretch the gap between the ratio values of shadow and nonshadow pixels. Based on the modified ratio map, our proposed STS applies a global thresholding

process to create a coarse-shadow map for classifying the input color aerial image into the candidate shadow pixels and the non-shadow pixels. In order to detect the true shadow pixels from the candidate shadow pixels, the connected component process is first performed to the candidate shadow pixels for grouping the candidate shadow regions. For each candidate shadow region, the local thresholding process is performed iteratively to extract the true shadow pixels from the candidate shadow region. Finally, for the remaining candidate regions, a fine-shadow determination process is presented to determine whether each remaining candidate shadow pixel is the true shadow pixel or not. Under six testing images, experimental results show that, for the first three testing images, both Tsai's and our proposed algorithms have better detection performance than that of the algorithm of Huang *et al.*, and the shadow detection accuracy of our proposed STS-based algorithm is comparable to Tsai's algorithm. For the other three testing images, which contain some low brightness objects, our proposed algorithm has better shadow detection accuracy when compared with the previous two shadow detection algorithms proposed by Huang *et al.* and Tsai.

The remainder of this paper is organized as follows. In Section II, we survey Tsai's shadow detection algorithm. In Section III, our proposed STS-based algorithm is presented. Section IV demonstrates the performance comparison among our proposed STS-based algorithm, Tsai's algorithm, and the algorithm of Huang *et al.* Section V addresses some concluding remarks.

II. PAST SHADOW DETECTION WORK BY TSAI

In this section, we survey the algorithm proposed by Tsai [12]. The flowchart of Tsai's algorithm is shown in Fig. 1. To detect shadows in the color aerial image, Tsai transforms the input *RGB* image I into an invariant color model, i.e., *HSI, HSV, HCV, YIQ,* or YC_bC_r color models. For each pixel, the ratio of the hue over the intensity is used to determine whether the pixel is a shadow pixel or not. For easy exposition, the *HSI* color model is used as the representative. Note that, among these five invariant color models, Tsai's algorithm has the best shadow detection performance for the *HSI* model. The following equation is given to transform the *RGB* color model into the *HSI* color model [13]:

$$\begin{bmatrix} I \\ V_1 \\ V_2 \end{bmatrix} = \begin{bmatrix} \frac{1}{3} & \frac{1}{3} & \frac{1}{3} \\ \frac{-\sqrt{6}}{6} & \frac{-\sqrt{6}}{6} & \frac{\sqrt{6}}{3} \\ \frac{1}{\sqrt{6}} & \frac{-2}{\sqrt{6}} & 0 \end{bmatrix} \begin{bmatrix} R \\ G \\ B \end{bmatrix}$$

$$S = \sqrt{V_1^2 + V_2^2}$$

$$H = \begin{cases} \tan^{-1}\left(\frac{V_2}{V_1}\right), & \text{if } V_1 \neq 1 \\ H \text{ is undefined}, & \text{otherwise.} \end{cases} \quad (1)$$

In the *HSI* color model, I and H components are called the intensity- and hue-equivalent components, respectively. By
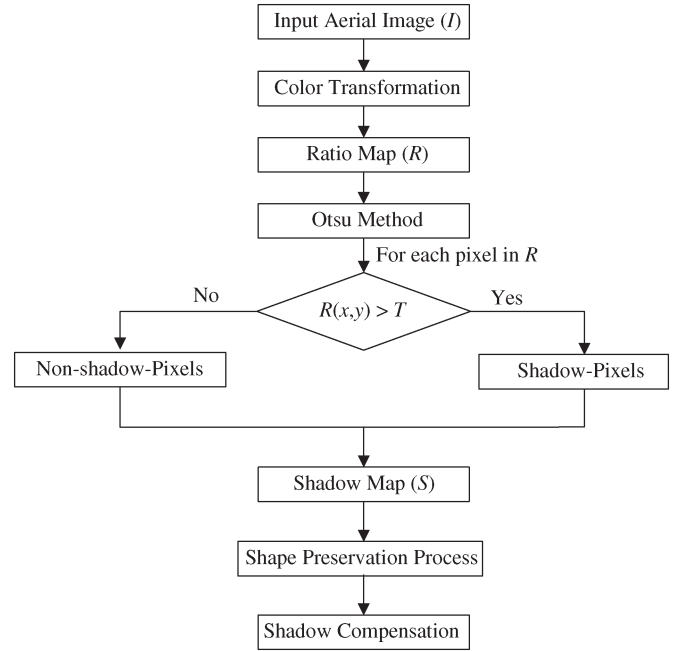

Fig. 1. Flowchart of Tsai's algorithm.

scaling I and H components to the range in [0, 1], we can obtain the intensity-equivalent image I_e and hue-equivalent image H_e, respectively. The ratio map R is defined by

$$R(x,y) = \frac{H_e(x,y) + 1}{I_e(x,y) + 1} \quad (2)$$

where $R(x,y)$, $H_e(x,y)$, and $I_e(x,y)$ denote the pixel at position (x,y) of R, the image H_e, and the image I_e, respectively. In Tsai's algorithm, the value of $R(x,y)$ is scaled to the range [0, 255] for shadow detection.

From the ratio map R, Otsu's thresholding method [14] is applied to determine the threshold T which can be used for separating all the pixels of R into two classes, where the threshold T is determined by

$$T = \arg\min_T \left(\sum_{i=0}^{T} P(i)(i-\mu_1)^2 + \sum_{i=T+1}^{255} P(i)(i-\mu_2)^2 \right) \quad (3)$$

where $P(i)$ denotes the probability of the ratio value i in R, $\mu_1 = \sum_{i=0}^{T}(iP(i)/W_1)$, and $\mu_2 = \sum_{i=T+1}^{255}(iP(i)/W_2)$, where $W_1 = \sum_{i=0}^{T} P(i)$ and $W_2 = \sum_{i=T+1}^{255} P(i)$. Based on the threshold T, a shadow map S can be obtained by

$$S(x,y) = \begin{cases} 1, & R(x,y) > T \\ 0, & \text{otherwise} \end{cases} \quad (4)$$

where $S(x,y) = 1$ denotes the shadow pixel at position (x,y).

Furthermore, Tsai presented a shape preservation process to preserve shape information of objects casting shadows. It first performs the Sobel operator on $I_e(x,y)$ to obtain the gradient map, and then, a shape map S_h can be constructed by applying Otsu's thresholding method to the gradient map. In the shape map S_h, the value of each pixel is determined by the similar

way as in (4). For each pixel $S_h(x,y)$, it is a boundary pixel of the casting object when $S_h(x,y) = 1$. After performing the logical AND operation on the shape map S_h and the shadow map S, the shape information of objects can be preserved. Finally, from the result of the shape preservation process, the shadow compensation process compensates shadows by adjusting the intensity values of shadow pixels. Since this paper focuses on the detection of shadows for color aerial images, the shadow compensation process is ignored.

III. OUR PROPOSED SHADOW DETECTION ALGORITHM

In this section, our proposed STS-based algorithm is presented to detect shadows for color aerial images. Instead of using the ratio map obtained by Tsai's algorithm, we present the modified ratio map to distinguish the candidate shadow pixels from nonshadow pixels. From the modified ratio map, the global thresholding process is first performed to obtain the coarse-shadow map, which separates all the pixels of the input image into candidate shadow pixels and nonshadow pixels. Furthermore, the local thresholding process is applied to each candidate shadow region in the coarse-shadow map iteratively to distinguish true shadow pixels from candidate shadow pixels. Finally, the fine-shadow determination process is applied to determine whether each pixel in the remaining candidate shadows is a true shadow pixel or not.

A. Proposed Modified Ratio Map

In Tsai's shadow detection algorithm, the ratio map R is obtained by using (2) to calculate the ratio value $R(x,y)$. However, for some cases, the two terms in (2), i.e., $H_e(x,y) + 1$ and $I_e(x,y) + 1$, may result in unsatisfactory shadow detection result since the values of $H_e(x,y)$ and $I_e(x,y)$ are scaled to the value in [0, 1]. For example, Fig. 2(a), (b), and (d) shows an input color aerial image, its ratio map obtained by Tsai's algorithm, and its shadow detection result, respectively. Note that the white pixels in Fig. 2(d) are the detected shadow pixels. We can observe that, in Fig. 2(b), the difference between the road and shadow regions is not large enough and the road regions are identified as the shadow regions in Fig. 2(d).

In order to overcome the aforementioned problem, we present a modified ratio map to improve the shadow detection accuracy. Based on the HSI color model, the intensity-equivalent image I_e and hue-equivalent image H_e used in the proposed modified ratio map are calculated by

$$I_e = \frac{1}{3}R + \frac{1}{3}G + \frac{1}{3}B \qquad (5)$$

$$H_e = \left(\tan^{-1}\left(\frac{V_2}{V_1}\right) + \pi\right) \times \frac{255}{2\pi} \qquad (6)$$

respectively, where V_1 and V_2 have been defined in (1) and the values of I_e and H_e are bounded in the range [0, 255]. The ratio value argument used in our modified ratio map is given by

$$r(x,y) = \text{round}\left(\frac{H_e(x,y)}{I_e(x,y) + 1}\right) \qquad (7)$$
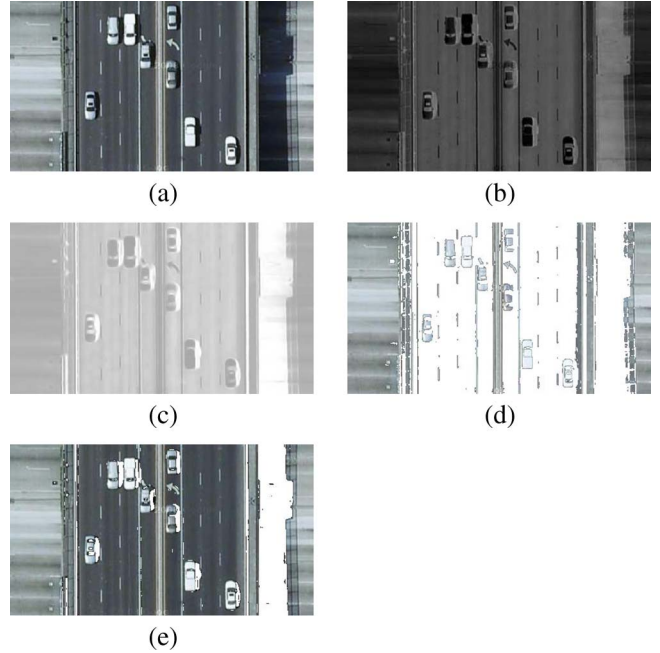

Fig. 2. Shadow detection comparison between the ratio map by Tsai and our modified ratio map. (a) Input color aerial image. (b) Tsai's ratio map of (a). (c) Our ratio map of (a). (d) Shadow detection result of (b). (e) Shadow detection result of (c).
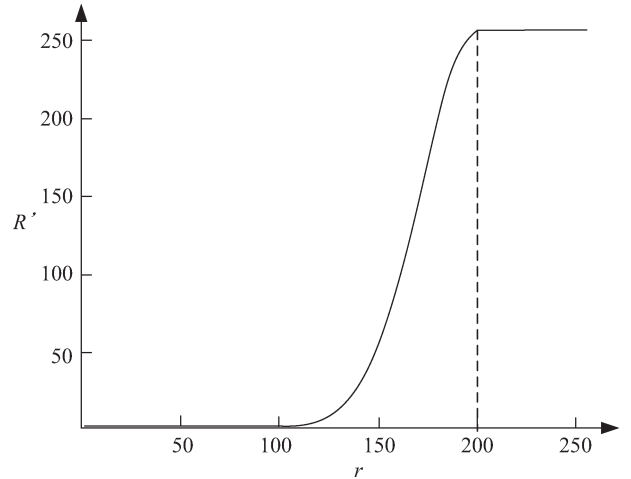

Fig. 3. Relationship between $r(x,y)$ and $R'(x,y)$, where T_S and σ are set to 200 and 20, respectively.

where the term $I_e(x,y) + 1$ can avoid dividing by zero, and the value of $r(x,y)$ can be bounded in the range [0, 255]. Our proposed modified ratio map R' is defined by

$$R'(x,y) = \begin{cases} e^{-\frac{(r(x,y)-T_S)^2}{4\sigma^2}} \times 255, & \text{if } r(x,y) < T_S \\ 255, & \text{otherwise.} \end{cases} \qquad (8)$$

In our implementation, the value of T_S is determined when the condition $\sum_{i=0}^{T_S} P(i) = P_S$ is held, where $P(i)$ denotes the probability of the ratio value i in $\{r(x,y)\}$; σ is calculated by $\sqrt{\sum_{i=0}^{T_S-1} P(i)(i - T_S)^2}$; and P_S is set to 0.95, empirically. In Fig. 3, the curve shows the relationship between $r(x,y)$ and $R'(x,y)$, where the values of T_S and σ are set to 200 and
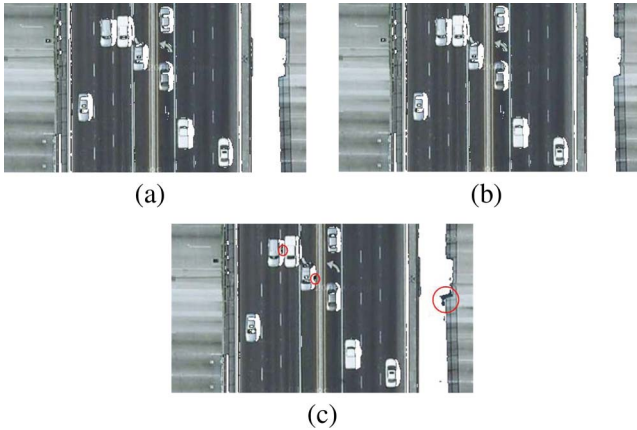
(a)

(b)

(c)

Fig. 4. Shadow detection results for different P_S's. (a) $P_S = 0.9$. (b) $P_S = 0.95$. (c) $P_S = 0.99$.
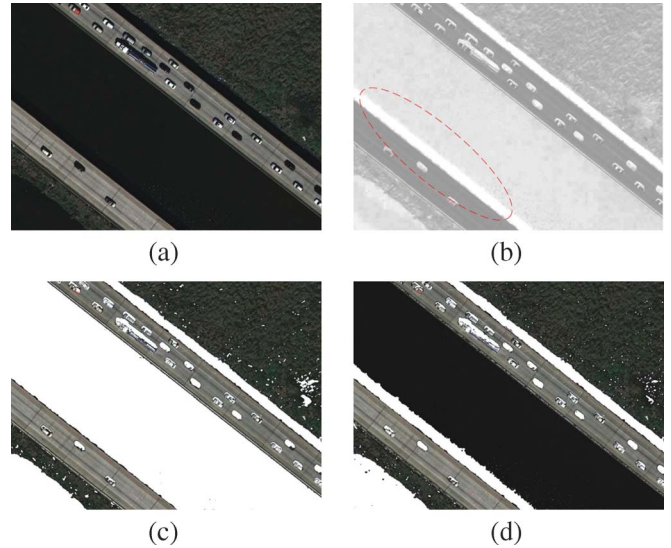

(a)

(b)

(c)

(d)

Fig. 5. Shadow detection comparison between the global thresholding scheme and our proposed STS. (a) Input color aerial image. (b) Modified ratio map of (a). (c) Shadow detection result of (a) by using the global thresholding scheme. (d) Shadow detection result of (a) by using the proposed STS.

20, respectively. In fact, the proposed modified ratio map in (8) can be used to replace the ratio map by Tsai to make the difference between the ratio values of the road regions and those of the shadow regions in the modified ratio map larger. Fig. 2(e) shows better detected shadows of Fig. 2(a) by putting the proposed modified ratio map into Tsai's algorithm. Here, the determination of P_S is based on the assumption that the ratio of the shadow-pixel number over the total pixel number in the input image is larger than $1 - P_S$. To determine an applicable P_S, a large value is set to P_S to construct the proposed modified ratio map since the number of the shadow pixels is much less than that of the nonshadow pixels for most color aerial images. Fig. 4(a)–(c) shows the shadow detection results for $P_S = 0.9$, $P_S = 0.95$, and $P_S = 0.99$, respectively. It is observed that both the detected results for $P_S = 0.90$ and $P_S = 0.95$ are satisfactory. However, when P_S is increased to 0.99, some shadow pixels are identified as the nonshadow pixels, which are denoted by the circled regions in Fig. 4(c), since the setting percentage of the number of the shadow pixels over that of the total pixels is too small and some shadow pixels cannot be detected. Based on all our testing images, $P_S = 0.95$ can detect many cases of shadows, but for some cases, the global thresholding process may lead to unsatisfactory results. In the next section, a new STS combining global and local thresholding processes is presented to improve the global thresholding process.

B. Proposed New STS

For some cases, it is hard to identify shadow regions from nonshadow regions even if the proposed modified ratio map has been considered in the shadow detection process. For example, Fig. 5(a) shows the input color aerial image, and Fig. 5(b) shows the modified ratio map of Fig. 5(a). In Fig. 5(b), the ratio submap surrounded by the dashed line includes the river and the roadway's shadow, and it seems that separating such a ratio submap into the shadow and nonshadow regions is easy. Based on the modified ratio map as shown in Fig. 5(b), the result of shadow detection carried out by using the global thresholding process is shown in Fig. 5(c). Surprisingly, the pixels within the river region are identified as shadow pixels even if the gap

between the ratio values of river region and roadway's shadow region is large.

In order to alleviate this problem, we now propose a new STS combining global and local thresholding processes to deal with such color aerial images. The flowchart of the proposed STS-based algorithm is shown in Fig. 6. In our proposed STS, based on the modified ratio map, the global thresholding process is first performed to obtain the coarse-shadow map, which separates the input image into candidate shadow pixels and nonshadow pixels. Based on the coarse-shadow map, the candidate shadow regions can be identified by using the connected component analysis [15], and then, we perform the local thresholding process to each region iteratively to detect true shadow pixels from candidate shadow pixels. Furthermore, we present a fine-shadow determination process to distinguish true shadows from candidate shadows, and then, we enforce the remaining candidate shadows to be the nonshadows. The detected shadows using our proposed STS-based algorithm are shown in Fig. 5(d). It reveals that the proposed algorithm has better accuracy than that of Tsai's algorithm.

Given an input *RGB* color aerial image I, we first transform I to the *HSI* color model by (1), and then, the modified ratio map R' can be obtained by (8). Furthermore, the anisotropic filter [16] is applied to R' to alleviate the noise effect without blurring the boundaries between candidate shadow regions and nonshadow regions. In order to refer more shadow information, the morphology dilation operator [15] with 3×3 square structuring elements is applied to R' to enlarge the candidate shadow regions. Under the obtained ratio map R', Otsu's method is used to determine a threshold T for constructing the coarse-shadow map S.

In our proposed STS-based algorithm, only the candidate shadow pixels are required to perform the local thresholding process to identify true shadow pixels. For the candidate shadow pixels in the coarse-shadow map, we construct candidate shadow regions by applying the connected component

```
                    ┌─────────────────────┐
                    │  Input Aerial Image │
                    └─────────────────────┘
                              │
                    ┌─────────────────────┐
                    │ Construct Modified  │
                    │    Ratio Map        │
                    └─────────────────────┘
                              │
                    ┌─────────────────────┐
                    │ Anisotropic Filtering│
                    └─────────────────────┘
                              │
                    ┌─────────────────────┐
                    │ Morphology Dilation │
                    └─────────────────────┘
                              │
                    ┌─────────────────────┐
                    │ Global Thresholding │
                    └─────────────────────┘
                              │
                    ┌─────────────────────┐
                    │  Coarse-Shadow Map  │
                    └─────────────────────┘
```
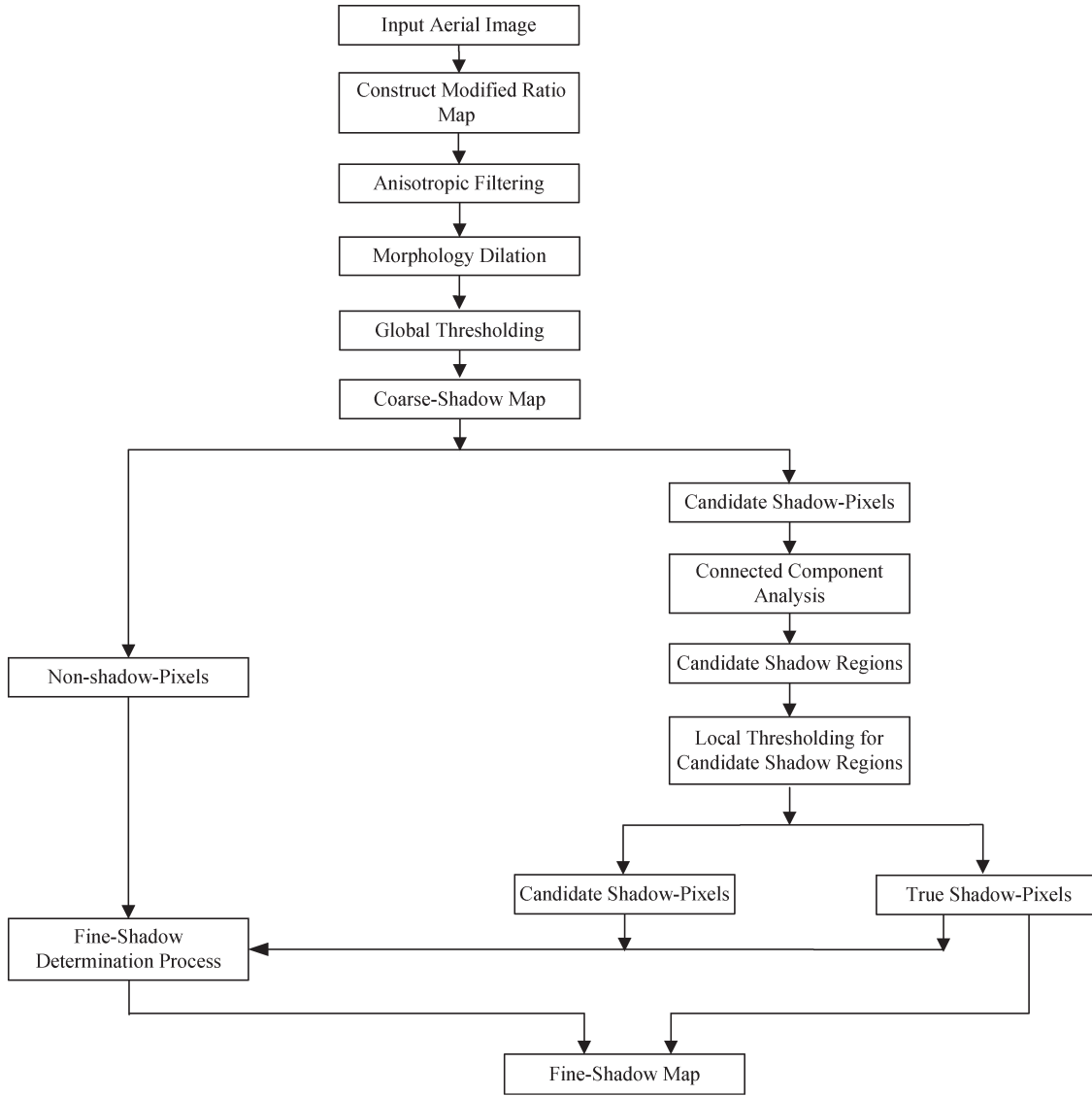
Fig. 6.   Flowchart of the proposed STS-based algorithm.

analysis to these pixels. Next, for each candidate shadow region, the local thresholding process is applied to distinguish true shadow pixels from candidate shadow pixels. Here, based on Otsu's thresholding method, the separability factor SP [17] is used to determine whether each candidate shadow region can be separated into the true shadow region and the candidate shadow region or not, and it is defined by

$$\text{SP} = \frac{\sigma_B^2}{\sigma_{T_L}^2} \qquad (9)$$

where $\sigma_B^2 = W_1(\mu_1 - \mu_{T_L})^2 + W_2(\mu_2 - \mu_{T_L})^2$ and $\sigma_{T_L}^2 = \sigma_B^2 + \sigma_W^2$ denote the between-class and total variances, respectively, when the candidate shadow region is binarized into two classes according to the threshold T_L obtained by Otsu's method; $W_1 = \sum_{i=0}^{T_L} P(i)$, and $W_2 = \sum_{i=T_L+1}^{255} P(i)$, where $P(i)$ denotes the probability of the ratio value i in R'; $\mu_1 = \sum_{i=0}^{T_L}(iP(i)/W_1)$, and $\mu_2 = \sum_{i=T_L+1}^{255}(iP(i)/W_2)$; and $\mu_{T_L} = W_1\mu_1 + W_2\mu_2$, and $\sigma_W^2 = W_1\sigma_1^2 + W_2\sigma_2^2$, where $\sigma_1^2 = \sum_{i=0}^{T_L} P(i)(i - \mu_1)^2$ and $\sigma_2^2 = \sum_{i=T_L+1}^{255} P(i)(i - \mu_2)^2$.
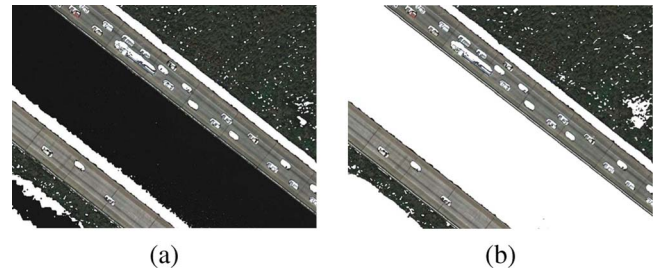

Fig. 7.   Shadow detection results for different T_{SP}'s by using our proposed STS. (a) $T_{SP} = 0.2$. (b) $T_{SP} = 0.8$.

For each candidate shadow region, if the condition SP $> T_{SP}$ is held where T_{SP} is set to 0.55, empirically, we separate the region into true shadows and candidate shadows according to the threshold T_L. A smaller T_{SP} tends to filter out more nonshadow pixels from each candidate shadow region. On the contrary, a larger T_{SP} tends to keep more true shadow pixels in the shadow detection result. Fig. 7 shows the influence of different T_{SP}'s on our proposed STS. Fig. 7(a) and (b) shows

the shadow detection results for $T_{SP} = 0.2$ and $T_{SP} = 0.8$, respectively. From Fig. 7(a), although the roadway's shadow region can be distinguished from the river region for $T_{SP} = 0.2$, in the bottom-left corner of the image, some true shadow pixels are identified as the nonshadow pixels. For $T_{SP} = 0.8$, Fig. 7(b) shows that more true shadow pixels in the bottom-left corner of the image are detected, but the river region is detected as the true shadow region. From the aforementioned analysis, medium T_{SP} is preferred. In our implementation, T_{SP} is set to 0.55, which is applicable to all our testing images [see one detected result shown in Fig. 5(d)].

Based on the detected candidate shadows, the proposed STS-based algorithm will be applied to them iteratively until all the true shadows have been detected. In our experiments, it is enough to call the STS-based algorithm twice. From the aforementioned description, our proposed STS can be described by the following successive thresholding procedure:

Procedure SuccessiveThresholding(I)
　　$\{I_e, H_e\} \leftarrow$ ColorTransform(I)
　　/* By (5) and (6) */
　　$R' \leftarrow$ ModifiedRatioImage(I) /* By (8) */
　　$H_{R'} \leftarrow$ Histogram(R')
　　/* Obtain the histogram of R' */
　　$T \leftarrow$ OtsuMethod($H_{R'}$)
　　/* Run Otsu's method on the histogram $H_{R'}^{*}$/
　　$P_{CS} \leftarrow \{\phi\}, P_N \leftarrow \{\phi\}$
　　/*P_{CS} is used to store candidate shadow pixels; P_N is used to store nonshadow pixels */
　　for each position (x, y) in R' **do**
　　　if $R'(x, y) > T$ **then**
　　　　$P_{CS} \leftarrow P_{CS} \cup (x, y)$
　　　　/* By (4), collect candidate shadow pixels*/
　　　else
　　　　$P_N \leftarrow P_N \cup (x, y)$
　　　　/* Collect nonshadow pixels */
　　$\{P_{CS}^0, P_{CS}^1, \ldots, P_{CS}^{n-1}\} \leftarrow$ ConnectedComponent(P_{CS})
　　/* Partition candidate shadow-pixels into a set of candidate shadow regions */
　　$P_S \leftarrow \{\phi\}$ /* P_S is used to store true shadow pixels */
　　for each $P_{CS}^i \in \{P_{CS}^0, P_{CS}^1, \ldots, P_{CS}^{n-1}\}$ **do**
　　　$P_S \leftarrow P_S \cup$ DetectShadow(P_{CS}^i, R',**True**)
　　　/* Procedure DetectShadow(P_{CS}^i, R', True) is used to extract true shadow pixels from candidate shadow region P_{CS}^i */
　　$P_{CS} \leftarrow P_{CS} \setminus P_S$
　　/* Collect the remaining candidate shadows for performing the fine-shadow determination process */
　　$P_S \leftarrow P_S \cup$ FineShadow($P_S, P_{CS}, P_N, I_e, H_e$)
　　/* The procedure FineShadow($P_S, P_{CS}, P_N, I_e, H_e$) is used to extract true shadows from candidate shadows */
　　return P_S

Implemented by the recursive manner, the subprocedure DetectShadow in the aforementioned procedure performs the local thresholding process to each candidate shadow region

iteratively for extracting true shadow pixels. The details of the subprocedure DetectShadow are shown after this paragraph. The subprocedure has three inputs P, R', and D, where P denotes the testing region, R' is the modified ratio map of the input image I, and D is used to identify whether the R' values of all pixels in the testing region are larger than the threshold or not in the previous thresholding process; if yes, we set $D =$ True, otherwise we set $D =$ False.

Subprocedure DetectShadow(P, R', D)
　　$H_{R'_L} \leftarrow$ LocalHistogram(P, R')
　　/* Obtain the histogram of testing region in the ratio map R' */
　　$T_L \leftarrow$ OtsuMethod($H_{R'_L}$)
　　/* Run Otsu's method on the histogram $H_{R'_L}$ */
　　$SP \leftarrow$ SeparabilityAnalysis($T_L, H_{R'_L}$)
　　/* Based on T_L, apply (9) to the histogram $H_{R'_L}$ */
　　$P_{S_L} \leftarrow \{\phi\}$
　　/*P_{S_L} is used to store the detected true shadow pixels */
　　if $SP > T_{SP}$ **then**
　　　$P_{CS_L} \leftarrow \{\phi\}$
　　　/*P_{CS_L} is used to store pixels whose R' values are not larger than T_L, i.e., store the candidate shadow pixels */
　　　for each position $(x, y) \in P$ **do**
　　　　if $R'(x, y) > T_L$ **then**
　　　　　$P_{S_L} \leftarrow P_{S_L} \cup (x, y)$
　　　　　/* By (4), collect pixels whose R' values are larger thanT_L */
　　　　else
　　　　　$P_{CS_L} \leftarrow P_{CS_L} \cup (x, y)$
　　　　　/* Collect pixels whose R' values are not larger than T_L */
　　　$\{P_{CS_L}^0, P_{CS_L}^1, \ldots, P_{CS_L}^{m'-1}\} \leftarrow$ ConnectedComponent (P_{CS_L})
　　　/* Partition pixels in P_{CS_L} into a set of regions */
　　　for each $P_{CS_L}^i \in \{P_{CS_L}^0, P_{CS_L}^1, \ldots, P_{CS_L}^{m'-1}\}$ **do**
　　　　$P_{S_L} \leftarrow P_{S_L} \cup$ DetectShadow($P_{CS_L}^i, R$, **False**)
　　　　/* The procedure DetectShadow($P_{CS_L}^i, R$, False) is used to extract true shadow pixels from the region $P_{CS_L}^i$ */
　　else
　　/* For the case that the testing region P cannot be separated, P is the true shadow region if all pixels in region P are larger than the threshold in the previous thresholding process and we set $D =$ True; otherwise, P is a candidate shadow region and we set $D =$ False */
　　　if $D =$ **True**
　　　　return P
　　　else
　　　　return $\{\phi\}$
　　return P_{S_L} /* Return detected true shadows */

C. Fine-Shadow Determination Process

After examining shadows in color aerial images, the following two properties are useful to distinguish true shadow pixels from nonshadow pixels.

Property 1: True shadow pixels usually have lower intensity values than that of the neighboring nonshadow pixels, but both of their chromaticity values are similar.

Property 2: For the color aerial images, most true shadow pixels are connected.

After running the connected component operation on the set of candidate shadow pixels P_{CS}, assume that we have n candidate shadow regions $P_{CS}^0, P_{CS}^1, P_{CS}^2, \ldots,$ and P_{CS}^{n-1}. Considering the ith candidate shadow region P_{CS}^i, $0 \leq i \leq n-1$, its mean intensity value is calculated by $\mu_{P_{CS}^i}^{I_e} = 1/|P_{CS}^i| \sum_{(x,y) \in P_{CS}^i} I_e(x,y)$, where $|P_{CS}^i|$ denotes the number of pixels in the candidate shadow region P_{CS}^i; the mean intensity value of its neighboring nonshadow pixels is calculated by $\mu_{P_{CS}^{i,N}}^{I_e} = 1/|P_{CS}^{i,N}| \sum_{(x,y) \in P_{CS}^{i,N}} I_e(x,y)$, where $P_{CS}^{i,N}$ denotes the set of neighboring nonshadow pixels which are five pixel wide around the candidate shadow region. The intensity values along the region boundaries are variant since they are influenced by the intensity values of both adjacent regions. In order to obtain a more accurate mean intensity value, the neighboring nonshadow pixels, which are about five pixel wide around the current candidate shadow region, have been considered. The following inequality

$$\mu_{P_{CS}^{i,N}}^{I_e} - \mu_{P_{CS}^i}^{I_e} > T_{I_e} \tag{10}$$

where the threshold T_{I_e} is set to 30, could be used to check whether the former condition of Property 1 is satisfied or not. The gap between the mean intensity value of each true shadow region and that of the neighboring nonshadow pixels, which are five pixel wide around the true shadow region, is denoted by T_{I_e}. T_{I_e} must be large enough to distinguish the true shadow region from the nonshadow region. However, if T_{I_e} is too large, some true shadow regions may not be detected. Based on our all testing images, $T_{I_e} = 30$ is a good separator for distinguishing the true shadow region from the nonshadow region.

Due to the intensity invariant property of the *HSI* color model, true shadow pixels and their neighboring nonshadow pixels have similar chromaticity values. Thus, the second condition of Property 1 can be checked by the following two inequalities:

$$\frac{\left| \mu_{P_{CS}^i}^{H_e} - \mu_{P_{CS}^{i,N}}^{H_e} \right|}{\sigma_{P_{CS}^i}^{H_e}} < T_\mu \tag{11}$$

$$\frac{\left| \sigma_{P_{CS}^i}^{H_e} - \sigma_{P_{CS}^{i,N}}^{H_e} \right|}{\sigma_{P_{CS}^i}^{H_e}} < T_\sigma \tag{12}$$

where, empirically, the two thresholds T_μ and T_σ are set to 1.5 and 0.6, respectively; $\mu_{P_{CS}^i}^{H_e}$ and $\mu_{P_{CS}^{i,N}}^{H_e}$ denote the mean H_e value of the ith candidate shadow region and the mean H_e value of its neighboring nonshadow pixels, respectively; and $\sigma_{P_{CS}^i}^{H_e}$ and $\sigma_{P_{CS}^{i,N}}^{H_e}$ denote the standard deviations of H_e values for

the ith candidate shadow region and its neighboring nonshadow pixels, respectively, and they are given by

$$\sigma_{P_{CS}^i}^{H_e} = \sqrt{\frac{1}{|P_{CS}^i|} \sum_{(x,y) \in P_{CS}^i} \left| H_e(x,y) - \mu_{P_{CS}^i}^{H_e} \right|^2}$$

$$\sigma_{P_{CS}^{i,N}}^{H_e} = \sqrt{\frac{1}{|P_{CS}^{i,N}|} \sum_{(x,y) \in P_{CS}^{i,N}} \left| H_e(x,y) - \mu_{P_{CS}^{i,N}}^{H_e} \right|^2}.$$

The usage of T_μ and T_σ is to determine whether the mean chromaticity value and standard deviation of each candidate shadow region and those of the neighboring nonshadow pixels, which are five pixel wide around the candidate shadow region, are similar or not, respectively. For smaller T_μ and T_σ, more candidate shadow regions are identified as the nonshadow regions, but some true shadow regions may be contained in these identified nonshadow regions. For all our testing images, $T_\mu = 1.5$ and $T_\sigma = 0.6$ are applicable for checking the second condition of Property 1.

If the candidate shadow region P_{CS}^i satisfies (11) and (12), it is said that the second condition of Property 1 is satisfied. From the aforementioned description, (10)–(12) can be used to determine whether each candidate shadow region satisfies Property 1 or not.

Return to Property 2. Let $P_{CS}^{i,S}$ and $P_{CS}^{i,N}$ denote the neighboring true shadow pixels and nonshadow pixels of the candidate shadow region P_{CS}^i, respectively. The following inequality is used to examine whether the candidate shadow region P_{CS}^i is connected to the true shadow pixels or not

$$\frac{|P_{CS}^{i,S}|}{|P_{CS}^{i,S}| + |P_{CS}^{i,N}|} > T_{CS} \quad (\leq 1) \tag{13}$$

where the threshold T_{CS} is set to 0.6 empirically. On the other hand, (13) can be used to examine whether Property 2 is held or not. For smaller T_{CS}, more candidate shadow regions are identified as the true shadow regions, but some nonshadow regions may be contained in these identified true shadow regions. In our experiments, $T_{CS} = 0.6$ is applicable to all our testing images.

For each candidate shadow region, if it satisfies Property 1 or Property 2, we regard it as the true shadow region; otherwise, this region is regarded as the nonshadow region. From our proposed fine-shadow determination process, the true shadow pixels can be extracted from the candidate shadow pixels. The aforementioned subprocedure FineShadow process is shown as follows.

Subprocedure FineShadow(P_S, P_{CS}, P_N, I_e, H_e)
  $P_{S_F} \leftarrow \{\phi\}$ /*P_{S_F} is used to store detected true shadow pixels */
  $\{P_{CS}^0, P_{CS}^1, \ldots, P_{CS}^{n-1}\} \leftarrow$ ConnectedComponent(P_{CS})
  /* Partition candidate shadow pixels into a set of candidate shadow regions */
  for each $P_{CS}^i \in \{P_{CS}^0, P_{CS}^1, \ldots, P_{CS}^{n-1}\}$ **do**
    $F_S \leftarrow$ **False**
    /* F_S is used to record whether P_{CS}^i is the true shadow

region ($F_S = $ **True**) or not ($F_S = $ **False**) */
$P_{\text{CS}}^{i,N} \leftarrow \text{NeighboringNonshadowPixels}(P_{\text{CS}}^i, P_N)$
/* Collect neighboring nonshadow pixels of P_{CS}^i */
Calculate $\mu_{P_{\text{CS}}^{i,N}}^{I_e}$ and $\mu_{P_{\text{CS}}^i}^{I_e}$ from $P_{\text{CS}}^{i,N}$ and P_{CS}^i

if $\mu_{P_{\text{CS}}^{i,N}}^{I_e} - \mu_{P_{\text{CS}}^i}^{I_e} > T_{I_e}$ **then**

    Calculate $\mu_{P_{\text{CS}}^i}^{H_e}, \mu_{P_{\text{CS}}^{i,N}}^{H_e}, \sigma_{P_{\text{CS}}^i}^{H_e}$, and $\sigma_{P_{\text{CS}}^{i,N}}^{H_e}$ from

    $P_{\text{CS}}^{i,N}$ and P_{CS}^i
    if $|\mu_{P_{\text{CS}}^i}^{H_e} - \mu_{P_{\text{CS}}^{i,N}}^{H_e}|/\sigma_{P_{\text{CS}}^i}^{H_e} < T_\mu$ and
       $|\sigma_{P_{\text{CS}}^i}^{H_e} - \sigma_{P_{\text{CS}}^{i,N}}^{H_e}|/\sigma_{P_{\text{CS}}^i}^{H_e} < T_\sigma$

    then
       $F_S \leftarrow$ **True**
       /* By (10), (11) and (12), if P_{CS}^i
       satisfies Property 1, it is identified as the true
       shadow region */
if $F_S = $ **False**
    $P_{\text{CS}}^{i,S} \leftarrow \text{NeighboringShadowPixels}(P_{\text{CS}}^i, P_S)$
    /* Collect neighboring true shadow pixels of P_{CS}^i */
    if $|P_{\text{CS}}^{i,S}|/|P_{\text{CS}}^{i,S}| + |P_{\text{CS}}^{i,N}| > T_{\text{CS}}$ **then**
       $F_S \leftarrow$ **True**
       /* By (13), if P_{CS}^i satisfies Property 2, it is
       identified as the true shadow region */
if $F_S = $ **True**
    $P_{S_F} \leftarrow P_{S_F} \cup P_{\text{CS}}^i$
return P_{S_F} /* Return detected true shadows */

IV. EXPERIMENTAL RESULTS

In this section, some experimental results are demonstrated to show the shadow detection accuracy comparison among the concerned three shadow detection algorithms, i.e., the algorithm of Huang *et al.* [11], Tsai's algorithm [12], and our proposed STS-based algorithm. All the concerned experiments are performed on the IBM compatible Pentium IV microprocessor with 3.2 GHz and 1-GB RAM. The operating system is MS-Windows XP, and the program developing environment is Borland C++ Builder 6.0. Our program has been uploaded in [18]. The following two sections are given to demonstrate the subjective and objective evaluations of the concerned three shadow detection algorithms.

Since our proposed STS-based algorithm consists of several processes, such as the construction of the modified ratio map, the global and local thresholding processes, and the fine-shadow determination process, it requires more execution time than the algorithm of Huang *et al.* and Tsai's algorithm.

A. Subjective Evaluation

Figs. 8(a)–13(a) show the six testing images, and the corresponding manually interpreted shadow maps, which are used as the ideal shadow maps to evaluate the shadow detection performance, are shown in Figs. 8(b)–13(b), respectively. The shadow detection results of the algorithm of Huang *et al.*, Tsai's algorithm, and our proposed STS-based algorithm are demonstrated in Figs. 8(c)–13(c), Figs. 8(d)–13(d), and Figs. 8(e)–13(e), respectively.
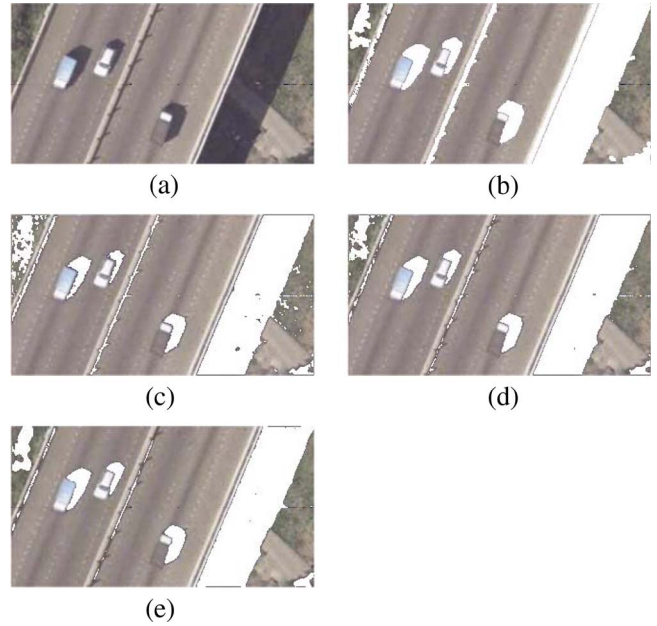

Fig. 8. Detection comparison among the concerned three algorithms for the first testing image. (a) Original image. (b) Ideal shadow detection result of (a). (c) Shadows detected by the algorithm of Huang *et al.* with $T_1 = -3$, $T_2 = 100$, and $T_3 = 120$. (d) Shadows detected by Tsai's algorithm. (e) Shadows detected by the proposed STS-based algorithm.
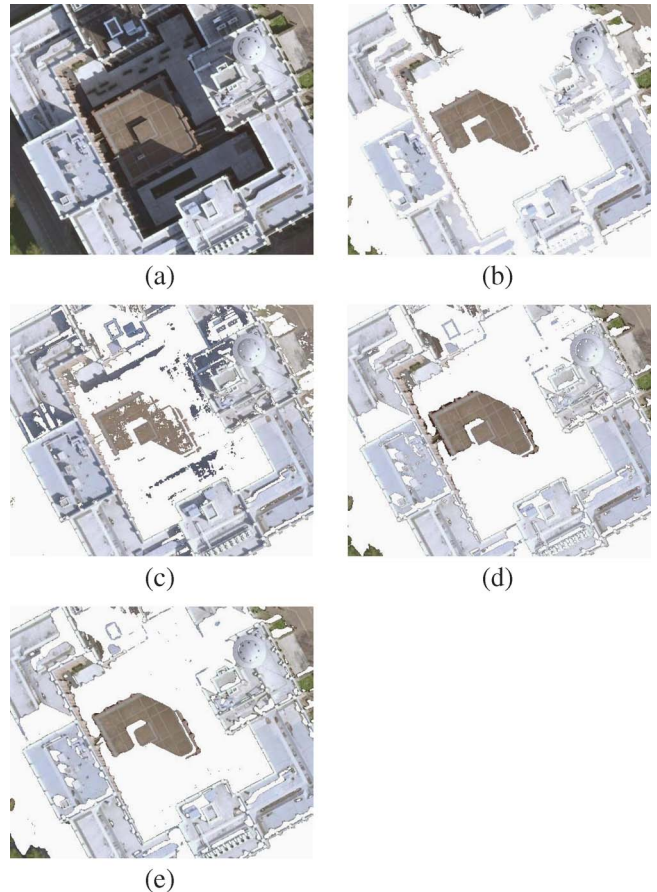

Fig. 9. Detection comparison among the concerned three algorithms for the second testing image. (a) Original image. (b) Ideal shadow detection result of (a). (c) Shadows detected by the algorithm of Huang *et al.* with $T_1 = -3$, $T_2 = 100$, and $T_3 = 120$. (d) Shadows detected by Tsai's algorithm. (e) Shadows detected by the proposed STS-based algorithm.
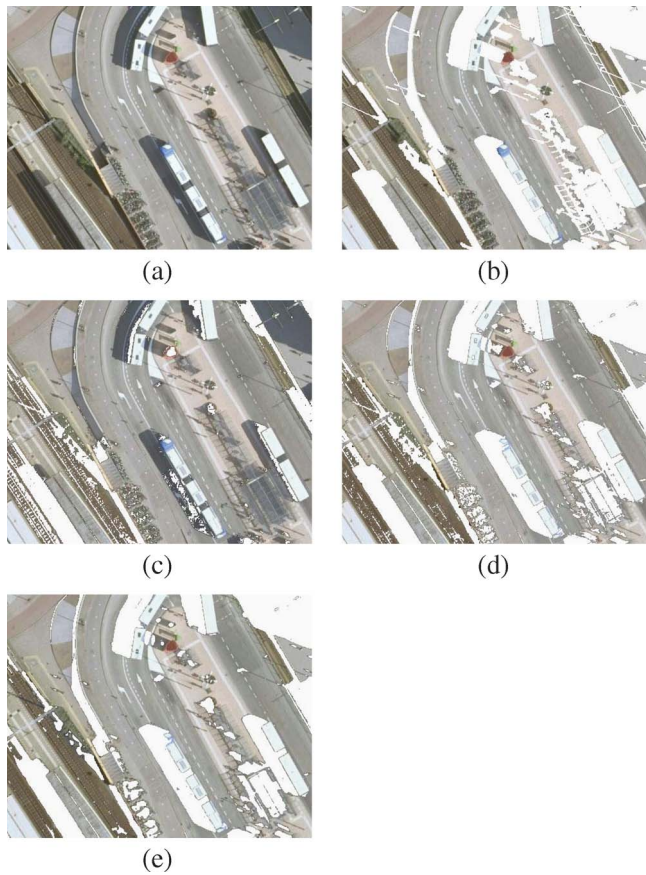
(a)

(b)

(c)

(d)

(e)

Fig. 10. Detection comparison among the concerned three algorithms for the third testing image. (a) Original image. (b) Ideal shadow detection result of (a). (c) Shadows detected by the algorithm of Huang *et al.* with $T_1 = -3$, $T_2 = 80$, and $T_3 = 120$. (d) Shadows detected by Tsai's algorithm. (e) Shadows detected by the proposed STS-based algorithm.

For the first three testing images as shown in Figs. 8(a)–10(a), the detected shadows by using both of Tsai's and the proposed STS-based algorithms are quite similar to the marked ideal shadows, as shown in Figs. 8(b)–10(b), respectively, and have better accuracy than the algorithm of Huang *et al.* For the other three testing images as shown in Figs. 11(a)–13(a), it is observed that our proposed STS-based algorithm has the best accuracy performance among the three concerned algorithms and the detected results by our proposed algorithm are close to the ideal shadows marked in Figs. 11(b)–13(b), respectively. From the detected shadows, we can observe that the greenward in Fig. 11(a), the river and the green lawn in Fig. 12(a), and the roadway in Fig. 13(a) are regarded as shadows by the algorithm of Huang *et al.* [see Figs. 11(c)–13(c)] and Tsai's algorithm [see Figs. 11(d)–13(d)]. In Figs. 11(e)–13(e), shadows can be detected correctly by our proposed STS-based algorithm. The aforementioned subjective evaluation demonstrates that our proposed STS-based algorithm has the best accuracy performance among the three algorithms.

B. Objective Evaluation

In this section, the objective evaluation metrics used in [12] are adopted to evaluate the accuracy of the concerned three shadow detection algorithms. Based on the concept of the
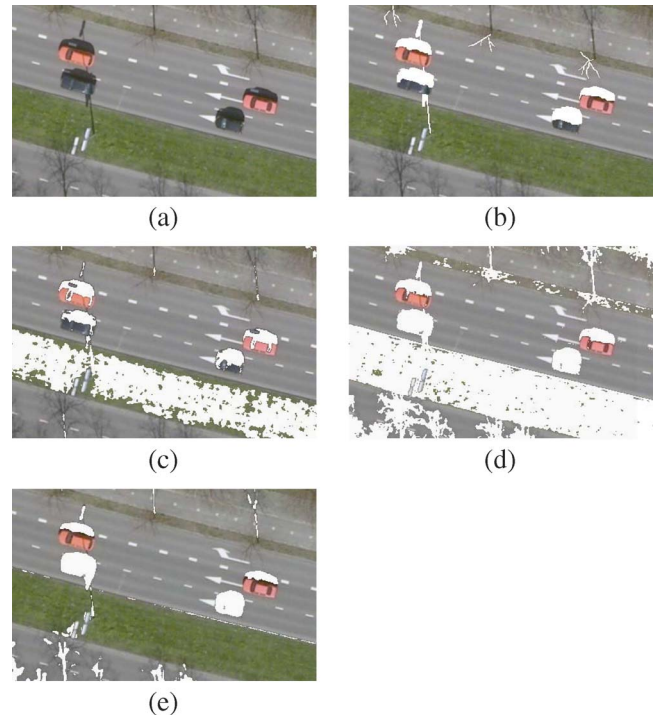

(a)

(b)

(c)

(d)

(e)

Fig. 11. Detection comparison among the concerned three algorithms for the fourth testing image. (a) Original image. (b) Ideal shadow detection result of (a). (c) Shadows detected by the algorithm of Huang *et al.* with $T_1 = -3$, $T_2 = 80$, and $T_3 = 120$. (d) Shadows detected by Tsai's algorithm. (e) Shadows detected by the proposed STS-based algorithm.

(a)

(b)

(c)

(d)

(e)

Fig. 12. Detection comparison among the concerned three algorithms for the fifth testing image. (a) Original image. (b) Ideal shadow detection result of (a). (c) Shadows detected by the algorithm of Huang *et al.* with $T_1 = -3$, $T_2 = 80$, and $T_3 = 120$. (d) Shadows detected by Tsai's algorithm. (e) Shadows detected by the proposed STS-based algorithm.

(a)   (b)

(c)   (d)
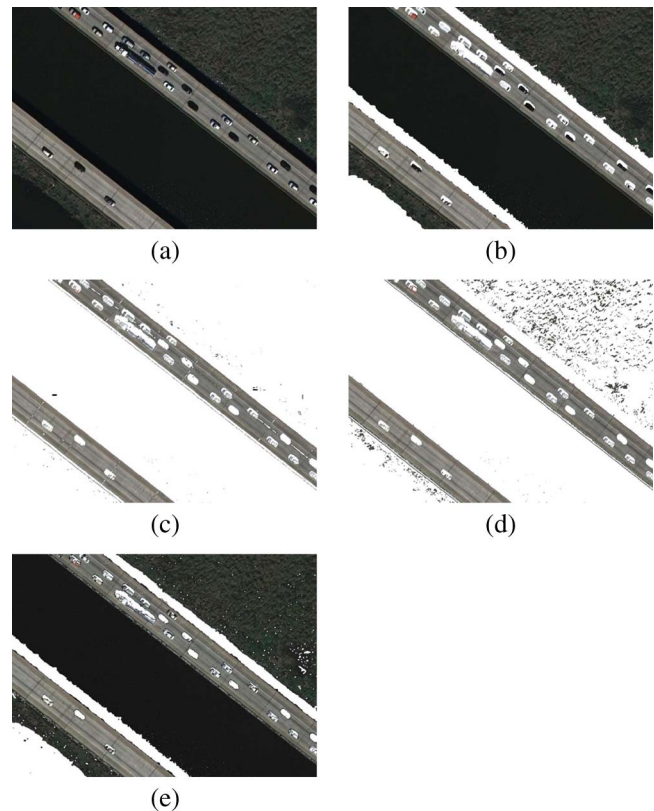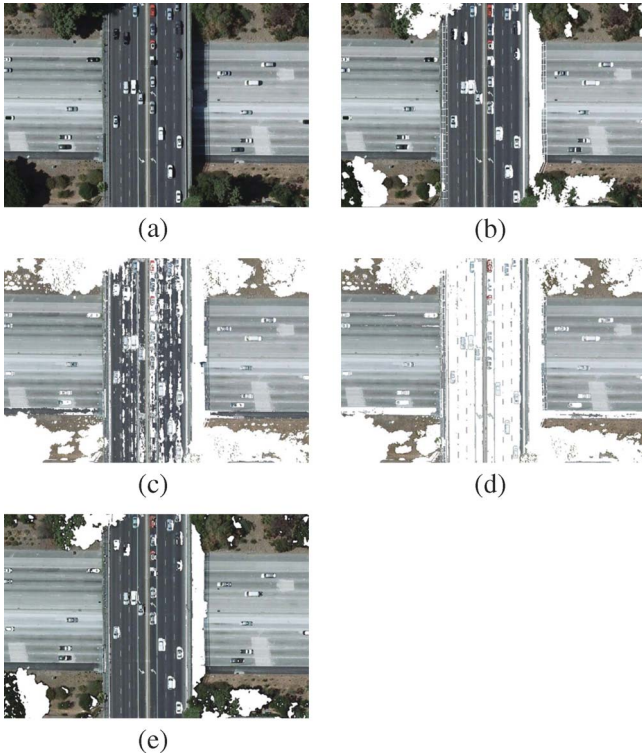
(e)

Fig. 13. Detection comparison among the concerned three algorithms for the sixth testing image. (a) Original image. (b) Ideal shadow detection result of (a). (c) Shadows detected by the algorithm of Huang et al. with $T_1 = -3$, and $T_2 = 80$, and $T_3 = 120$. (d) Shadows detected by Tsai's algorithm. (e) Shadows detected by the proposed STS-based algorithm.

TABLE I
THREE SHADOW DETECTION ACCURACY MEASUREMENTS FOR FIG. 8(a)

Method	Producer's accuracies		User's accuracies		Overall accuracies
	$\eta_s(\%)$	$\eta_n(\%)$	$p_s(\%)$	$p_n(\%)$	$\tau(\%)$
Proposed	92.21	98.83	95.63	97.57	97.16
Tsai's	92.15	98.97	96.16	97.82	97.47
Huang et al.'s	92.13	98.13	93.25	97.80	96.81

TABLE II
THREE SHADOW DETECTION ACCURACY MEASUREMENTS FOR FIG. 9(a)

Method	Producer's accuracies		User's accuracies		Overall accuracies
	$\eta_s(\%)$	$\eta_n(\%)$	$p_s(\%)$	$p_n(\%)$	$\tau(\%)$
Proposed	85.96	97.96	98.01	85.57	91.44
Tsai's	86.23	97.84	97.90	85.88	91.59
Huang et al.'s	70.21	94.78	94.01	73.14	81.54

TABLE III
THREE SHADOW DETECTION ACCURACY MEASUREMENTS FOR FIG. 10(a)

Method	Producer's accuracies		User's accuracies		Overall accuracies
	$\eta_s(\%)$	$\eta_n(\%)$	$p_s(\%)$	$p_n(\%)$	$\tau(\%)$
Proposed	73.33	97.50	92.00	90.30	90.68
Tsai's	75.85	96.13	88.50	91.02	90.41
Huang et al.'s	27.30	96.03	73.00	77.06	76.63

error matrices [1], [2] and the terminologies defined in [19], [20], three types of accuracy, namely the producer's accuracy, the user's accuracy, and the overall accuracy, are used in the objective evaluation.

The three types of accuracy are described as follows. The first type of accuracy is the producer's accuracy, which contains two parameters ηs and ηn, and they are defined by

$$\eta s = \frac{TP}{TP + FN}$$

$$\eta n = \frac{TN}{FP + TN}$$

where true positive (TP) denotes the number of true shadow pixels which are identified correctly; false negative (FN) denotes the number of true shadow pixels which are identified as nonshadow pixels; false positive (FP) denotes the number of nonshadow pixels which are identified as true shadow pixels; and true negative (TN) is the number of nonshadow pixels which are identified correctly. The parameter ηs (ηn) denotes the ratio of the number of correctly detected true shadow (nonshadow) pixels over that of total true shadow (nonshadow) pixels. The second type of accuracy is the user's accuracy in terms of ps and pn, which are defined as

$$ps = \frac{TP}{TP + FP}$$

$$pn = \frac{TN}{TN + FN}$$

The parameter ps (pn) denotes the ratio of the number of correctly detected true shadow (nonshadow) pixels over that of the total detected true shadow (nonshadow) pixels, and thus, the user's accuracy can be used to measure the precision of the shadow detection algorithm. Combining the accuracies of the user and the producer, the third type of accuracy τ defined as follows can be used to evaluate the correctness percentage [2] of the algorithm:

$$\tau = \frac{TP + TN}{TP + TN + FP + FN}$$

where $TP + TN$ denotes the number of correctly detected true shadow and nonshadow pixels; $TP + TN + FP + FN$ is equal to the number of total pixels in the image.

From the aforementioned three types of accuracy, Tables I–VI show the accuracy comparison among the algorithm of Huang et al., Tsai's algorithm, and our STS-based algorithm for Figs. 8(a)–13(a), respectively. In Tables I–III, the accuracy of the proposed STS-based algorithm is very close to that of Tsai's algorithm, and both two algorithms have better accuracy than the algorithm of Huang et al. Tables IV–VI demonstrated that our proposed STS-based algorithm has better accuracy performance when compared with the other two algorithms.

TABLE IV
THREE SHADOW DETECTION ACCURACY MEASUREMENTS FOR FIG. 11(a)

Method	Producer's accuracies		User's accuracies		Overall accuracies
	$\eta_s(\%)$	$\eta_n(\%)$	$p_s(\%)$	$p_n(\%)$	$\tau(\%)$
Proposed	74.49	97.08	46.50	99.11	96.33
Tsai's	89.14	64.26	7.85	99.43	65.08
Huang *et al.*'s	85.21	80.1	8.28	99.61	80.21

TABLE V
THREE SHADOW DETECTION ACCURACY MEASUREMENTS FOR FIG. 12(a)

Method	Producer's accuracies		User's accuracies		Overall accuracies
	$\eta_s(\%)$	$\eta_n(\%)$	$p_s(\%)$	$p_n(\%)$	$\tau(\%)$
Proposed	93.36	98.93	92.21	99.1	98.27
Tsai's	99.66	27	15.56	99.83	35.64
Huang *et al.*'s	99.57	22.41	14.76	99.74	31.58

TABLE VI
THREE SHADOW DETECTION ACCURACY MEASUREMENTS FOR FIG. 13(a)

Method	Producer's accuracies		User's accuracies		Overall accuracies
	$\eta_s(\%)$	$\eta_n(\%)$	$p_s(\%)$	$p_n(\%)$	$\tau(\%)$
Proposed	82.97	98.42	85.81	98.04	96.81
Tsai's	99.86	58.40	21.72	99.97	62.7
Huang *et al.*'s	99.4	75.51	31.93	99.91	77.99

Overall, besides the subjective evaluation advantage, the objective evaluation also demonstrated the shadow detection advantage of our proposed STS-based algorithm when compared with the algorithm of Huang *et al.* and Tsai's algorithm.

V. CONCLUSION

In this paper, based on the coarse-to-fine strategy, our proposed STS-based algorithm has been presented for detecting shadows of color aerial images. Based on the proposed modified ratio map, the coarse-shadow map is constructed by using the global thresholding process. From the coarse-shadow map, our proposed STS first classifies all the pixels into the true and candidate shadow types. Furthermore, the proposed fine-shadow determination process is used to distinguish the true shadows from the candidate shadows. Experimental results demonstrated that our proposed STS-based algorithm has better shadow detection accuracy when compared with the algorithm of Huang *et al.* and Tsai's algorithm.

ACKNOWLEDGMENT

The authors would like to thank Prof. V. J. D. Tsai for providing the experimental results by running the shadow detection algorithm in [12] on the testing images that lead to the improved presentation of this paper.

REFERENCES

[1] T. M. Lillesand and R. W. Kiefer, *Remote Sensing and Image Interpretation*, 4th ed. New York: Wiley, 2000.
[2] W. R. Philipson, *Manual of Photographic Interpretation*, 2nd ed. Bethesda, MD: Amer. Soc. Photogrammetry Remote Sens., 1997.
[3] A. Huertas and R. Nevatia, "Detecting buildings in aerial images," *Comput. Vis. Graph. Image Process.*, vol. 41, no. 2, pp. 131–152, Feb. 1988.
[4] Y. Liow and T. Pavlidis, "Use of shadows for extracting buildings in aerial images," *Comput. Vis. Graph. Image Process.*, vol. 49, no. 2, pp. 242–277, Feb. 1990.
[5] S. Watanabe, K. Miyajima, and N. Mukawa, "Detecting changes of buildings from aerial images using shadow and shading model," in *Proc. 14th Int. Conf. Pattern Recog.*, 1998, vol. 2, pp. 1408–1412.
[6] V. J. D. Tsai, "Automatic shadow detection and radiometric restoration on digital aerial images," in *Proc. Int. Geosci. Remote Sens. Symp.*, Toulouse, France, Jul. 21–25, 2003, pp. 732–733.
[7] C. Jiang and M. Ward, "Shadow identification," in *Proc. IEEE Conf. Comput. Vis. Pattern Recog.*, 1992, pp. 606–612.
[8] C. Jaynes, "Dynamic shadow removal from front projection displays," in *Proc. IEEE Conf. Vis.*, 2001, pp. 175–182.
[9] G. Finlayson, S. Hordley, and M. Drew, "Removing shadows from images," in *Proc. Eur. Conf. Comput. Vis.*, 2002, pp. 823–836.
[10] A. M. Polidorio, F. C. Flores, N. N. Imai, A. M. G. Tommaselli, and C. Franco, "Automatic shadow segmentation in aerial color images," in *Proc. XVI Brazilian Symp. Comput. Graph. Image Process.*, Oct. 12–15, 2003, pp. 270–277.
[11] J. Huang, W. Xie, and L. Tang, "Detection of and compensation for shadows in colored urban aerial images," in *Proc. 5th World Congr. Intell. Control Autom.*, Hangzhou, China, Jun. 15–19, 2004, pp. 3098–3100.
[12] V. J. D. Tsai, "A comparative study on shadow compensation of color aerial images in invariant color models," *IEEE Trans. Geosci. Remote Sens.*, vol. 44, no. 6, pp. 1661–1671, Jun. 2006.
[13] W. K. Pratt, *Digital Image Processing*, 2nd ed. New York: Wiley.
[14] N. Otsu, "A threshold selection method from gray-level histograms," *IEEE Trans. Syst., Man, Cybern.*, vol. SMC-9, no. 1, pp. 62–69, Jan. 1979.
[15] R. C. Gonzalez and R. E. Woods, *Digital Image Processing*, 2nd ed. Reading, MA: Addison-Wesley, 2002.
[16] G. Z. Yang, D. N. Firmin, P. Burger, and S. R. Underwood, "Structure adaptive anisotropic image filtering," *Image Vis. Comput.*, vol. 14, no. 2, pp. 135–145, Mar. 1996.
[17] H. H. Oh, K. T. Lim, and S. I. Chien, "An improved binarization algorithm based on a water flow model for document image with inhomogeneous backgrounds," *Pattern Recognit.*, vol. 38, no. 12, pp. 2612–2625, Dec. 2005.
[18] [Online]. Available: http://140.118.175.164/Huang/STS-Based Algorithm.zip
[19] A. Prati, I. Mikic, M. M. Trivedi, and R. Cucchiara, "Detecting moving shadows: Algorithms and evaluation," *IEEE Trans. Pattern Anal. Mach. Intell.*, vol. 25, no. 7, pp. 918–923, Jul. 2003.
[20] J. Yao and Z. Zhang, "Systematic static shadow detection," in *Proc. 17th Int. Conf. Pattern Recog.*, 2004, vol. 2, pp. 76–79.

Kuo-Liang Chung (M'91–SM'01) received the B.S., M.S., and Ph.D. degrees in computer science and information engineering from the National Taiwan University, Taipei, Taiwan, in 1982, 1984, and 1990, respectively.

He was a Visiting Scholar at the University of Washington, Seattle, in the summer of 1999. From 2003 to 2006, he was the Head of the Department of Computer Science and Information Engineering, National Taiwan University of Science and Technology, where he is currently a Professor. He was the Executive Editor of the *Journal of the Chinese Institute of Engineers* from 1996 to 1998. He has authored and coauthored over 130 publications in books and international well-known journals. His research interests include image/video compression and processing, pattern recognition, artificial intelligence, algorithms, and multimedia applications.

Dr. Chung received the Distinguished Engineering Professor Award from the Chinese Institute of Engineers in 2001; the Distinguished Research Award (from 2004 to 2007) from the National Science Council, Taiwan; and the best paper award from the Society of Computer Vision, Graphics, and Image Processing (Taiwan) in 2007. He is a Fellow of the Institution of Engineering and Technology.

Yi-Ru Lin received the B.S. degree in mathematics and computer science education from the Taipei Municipal University of Education, Taipei, Taiwan. She is currently working toward the M.S. degree in computer science and information engineering from National Taiwan University of Science and Technology, Taipei.

Her research interests include image processing and multimedia applications.

Yong-Huai Huang received the B.S. degree in information management from Aletheia University, Tamsui, Taipei, Taiwan, and the M.S. and Ph.D. degrees in computer science and information engineering from the National Taiwan University of Science and Technology, Taipei.

He is currently a Postdoctoral Researcher in the Department of Computer Science and Information Engineering, National Taiwan University of Science and Technology. His research interests include image processing and compression, and algorithms.